Constructing uniform sub-3 nm PtZn intermetallic nanocrystals via atomic layer deposition for fuel cell oxygen reduction

Chaojun Huang [a,b,1], Hang Liu [c,1], Yuanting Tang [c], Qizi Lu [a,b], Shengqi Chu [d], Xiao Liu [a,*], Bin Shan [b,c], Rong Chen [a,b,**]

[a] *State Key Laboratory of Digital Manufacturing Equipment and Technology, School of Mechanical Science and Engineering, Huazhong University of Science and Technology, Wuhan 430074, Hubei, People's Republic of China*
[b] *China-EU Institute for Clean and Renewable Energy, Huazhong University of Science and Technology, Wuhan 430074, Hubei, People's Republic of China*
[c] *State Key Laboratory of Materials Processing and Die & Mould Technology, School of Materials Science and Engineering, Huazhong University of Science and Technology, Wuhan 430074, Hubei, People's Republic of China*
[d] *Institute of High Energy Physics, Chinese Academy of Sciences, 100049 Beijing, People's Republic of China*

ARTICLE INFO

ABSTRACT

The preparation of ultra-small structurally ordered Pt-based intermetallic nanocrystals (< 3 nm) is still challenging due to the sintering during high temperature ordering. We report a strategy to construct size and distribution controllable Pt-based intermetallic nanocrystals based on ultra-thin metal oxide coating on Pt nanoparticles via atomic layer deposition. The area-selective and thickness controllable metal oxide coatings can not only provide metal atoms for alloying, but also prevent the sintering of Pt nanoparticles during subsequently fast ordering reduction. The prepared uniform PtZn intermetallic nanocrystals with the size of 2.50 ± 0.65 nm achieve outstanding single-cell performance with the mass activity of 0.48 A mg_{Pt}^{-1} at 0.9 V and 10.42 % loss of mass activity after 30,000 voltage cycles, which is superior to commercial Pt/C. The enhanced activity and durability is attributed to the decreased binding energy of Pt-oxygen intermediates for weakly polarized surface Pt atoms and suppressed electrochemical Ostwald ripening.

1. Introduction

Proton exchange membrane fuel cells (PEMFCs) are highly regarded for their high energy conversion efficiency and zero emissions in addressing the current severe energy and environmental crises [1–3]. Reducing noble Pt usage in catalysts of oxygen reduction reaction (ORR) with sluggish kinetics is still the key point for the commercialization of PEMFCs. Alloying Pt with inexpensive transition metals (Cu, Fe, Zn, Co, Ni, Cr, etc.) is a viable and heavily explored strategy, which can exploit the strong coupling between the 3*d* and 5*d* atomic orbitals of transition metals and Pt to weaken the binding of intermediate oxygen species and accelerate ORR kinetics [4–10]. In order to avoid the leaching of transition metal in acid condition, Pt-based intermetallic nanocrystals with long range ordered intermetallic core structure have aroused much attention, which requires 700 °C or even higher temperature to

overcome the energy barrier of atomic diffusion and ordering for Pt alloys and exhibits enhanced stability [11–13]. Although the temperature for mobility of host matrix atoms can be decreased by the addition of some metal dopants [14], high temperature ordering is the common process to prepare fully ordered nanocrystals, which will inevitably trigger the sintering and agglomeration of the intermetallic nanocrystals, resulting in large average size (> 5 nm) and broad size distribution of the most reported ordered Pt-based intermetallic catalysts [15–17].

To increase noble Pt utilization, many effective strategies are developed to confront the sintering and growing up of Pt-based intermetallic nanocrystals during the disorder to order transition, which can be divided into two types according to their focused objects (carbon-based supports or Pt-based nanoparticles) [18–20]. One is specifically engineering carbon-based supports with special confined structure or

---

surface anchoring defects to handle the sintering problem of supported Pt-based nanoparticles [21–24]. By introducing sulfocompound into carbon supports, the sulfur dopants can strongly interact with Pt and transition metal atoms to help suppress sintering during high temperature ordering [25]. Although this type of approach is practical in controlling the growth of Pt nanocrystals, the distributions of Pt and transition metal precursors on supports can be directly influenced by solvent effect and the locations of anchor ligands or structural traps. The inhomogeneous distribution of Pt and transition metal precursors usually leads to a broad size distribution of Pt-based intermetallic nanocrystals, which can accelerate Ostwald ripening during electrochemical reactions [26–28]. Another type of approach is developed by introducing organic macromolecule coating or oxide shell to prevent the aggregation of Pt based nanoparticles during wet chemical synthesis and high temperature ordering, such as polydopamine, oleylamine, Al_2O_3, MgO or SiO_2 [29–31]. It is suitable for the synthetic approaches that start from alloying between Pt and transition metals, including microwave-assisted alcohol-reduction process, seed mediated method, controlled decomposition and reduction of metal-organic precursors, etc [32–35]. For instance, Pt nanoparticles with protective MgO shell are prepared layer by layer from inside-out by hot-injection method in organic solvent. Structurally ordered intermetallic nanocrystals can be produced after annealing at 700 °C and subsequently pickling to remove MgO shell [36]. Since the strongly chemical binding of organic macromolecule on Pt and difficult thickness control of oxide shell, it is very hard to clean them up thoroughly, which can reduce the electrochemical active surface area (ECSA) of Pt and weaken the interaction between Pt nanocrystal and supports. Overall, it is still challenging to prepare ultra-small Pt-based intermetallic nanocrystals with uniform size distribution and strong interaction between Pt nanocrystals and supports, which are of great significance for the activity and stability of Pt catalysts.

Herein, we report a well-designed strategy to construct ultra-small Pt-based intermetallic nanocrystals by selectively ultra-thin metal oxide coating on Pt nanoparticles via atomic layer deposition (ALD) and subsequently fast ordering reduction. The ultra-thin ZnO coating has been chosen to provide Zn atoms for alloying with Pt nanocrystals and prevent the sintering during ordering reduction at 800 °C. Uniform PtZn intermetallic nanocrystals are obtained with the size of 2.50 ± 0.65 nm, which exhibit excellent activity and durability for oxygen reduction reaction in acidic media. The outstanding single-cell performance is achieved compared to that of commercial Pt/C, which can be attributed to the decreased binding energy of Pt-oxygen intermediates and suppressed electrochemical Ostwald ripening for uniform PtZn intermetallic nanocrystals.

2. Experimental and computational methods

2.1. Synthesis of catalysts

The carbon-supported Pt/C was prepared using an impregnation reduction method. In a typical synthesis, 140 μL of $Pt(NO_3)_2$ solution (18 wt%) and 400 mg of Vulcan XC-72 carbon support were dispersed in 20 mL deionized water. The mixture was subjected to ultrasonic treatment for 1 h before drying by using a rotary evaporator at 80 °C. After being ground in an agate mortar, the dried and free-flowing powder was heated in a tube furnace at 600 °C under a mixture of Ar + 10% H_2 with a heating rate of 5 °C min^{-1} for 1 h. The theoretical platinum loading of prepared Pt/C was 10 wt%. Then the zinc oxide protective shell was selectively deposited by custom-made fluidized-bed reactor. We used diethylzinc and oxygen as precursors. The bottle of precursor (Zn (CH$_2$CH$_3$)$_2$) was kept at room temperature 25 °C. The gas line was heated to 80 °C and the reactor temperature was fixed at 80 °C. Nitrogen gas (99.999 % in purity) was used as a carrier gas at a flow rate of 200 sccm. One ALD cycle was executed with the completion of the following four steps: (1) a 90 s supply of Zn(CH$_2$CH$_3$)$_2$; (2) a 120 s purge of N$_2$; (3)

a 90 s supply of O$_2$; (4) a 120 s purge of N$_2$. After repeating the above ALD process for 5 cycles, the obtained sample was named Pt@ZnO/C. After ZnO deposition, the sample Pt@ZnO/C was rapidly annealed at 800 °C under Ar + 10 % H_2 with a heating rate of 5 °C min^{-1} for 1 h. After cooling to room temperature, the sample was collected and denoted as PtZn/C-ALD. As a comparison, we also used the incipient wetness impregnation (IWI) method to synthesize carbon supported PtZn intermetallic nanocrystals, denoted as PtZn/C-IWI. In a typical synthesis, the molar ratio of Pt precursor (Pt(NO$_3$)$_2$) and Zn precursor (Zn(NO$_3$)$_2$·6H$_2$O) were controlled at 1:1. 140 μL of Pt(NO$_3$)$_2$ solution (18 wt%), 41.38 mg of Zn(NO$_3$)$_2$·6(H$_2$O) and 400 mg of Vulcan XC-72 carbon support were dispersed in 20 mL deionized water. The mixture was subjected to ultrasonic treatment for 1 h before drying by using a rotary evaporator at 80 °C. After being ground in an agate mortar, the dried and free-flowing powder was heated in a tube furnace at 800 °C under a mixture of Ar + 10 % H_2 with a heating rate of 5 °C min^{-1} for 1 h.

2.2. Characterization

The X-ray diffraction (XRD) spectra of the catalysts were characterized by PANalytical X′Pert Pro with a Cu $K_{\alpha 1}$ radiation source in the 2θ range of 10–80°. The structure and elements distribution of Pt nanoparticles on carbon support, ZnO shell coated on Pt nanoparticles and ultra-small PtZn intermetallic nanoparticles were characterized via transmission electron microscopy and scanning transmission electron microscopy (TEM and STEM, Talos F200X, FEI) coupled with energy dispersive spectroscopy (EDS). The X-ray absorption fine structure (XAFS) spectra were performed at the 1W1B beamline of Beijing synchrotron radiation facility. The Pt L$_3$-edge of Pt/C, Pt@ZnO/C and PtZn/C-ALD catalysts were collected in transmission mode with the energy range of 11368–12463 eV. The Pt L$_3$-edge of Pt foil and PtO$_2$ were tested as references. By considering the parameters of coordinated number (N), bond length (R, Å), Debye-Waller factor (σ^2, Å^2) and shift in the edge energy (ΔE$_0$, eV), the Pt k^2-weighted Fourier-transformed extended X-ray absorption fine structure (EXAFS) spectrum of catalysts was fitted by using the Pt foil, PtO$_2$ and PtZn modes in Demeter program. Wavelet transform (WT) EXAFS analyses were provided, which can discriminate the backscattering atoms and provide powerful resolution in k space and R space. The chemical states of catalysts were analyzed on an X-ray photoelectron spectrometer (XPS, AXIS-ULTRA DLD-600 W) purchased from Kratos using Al K_α radiation. All XPS spectra were calibrated based on the peak position of C 1s (284.8 eV). FTIR spectra were collected by wide band mercury cadmium telluride detector on the Nicolet iS50 FTIR spectrometer (Thermo Fisher Scientific) to elucidate the deposition behaviors of ZnO on Pt nanoparticles. The mass loading of Pt and Zn were determined by inductively coupled plasma atomic emission spectrometer (ICP-OES, Avio 220 Max, PerkinElmer).

2.3. Electrochemical measurements

The electrochemical measurements were performed by a CHI 760E electrochemical workstation at room temperature. A three-electrode electrochemical setup with a rotating disk electrode (RDE) system was used. A glassy carbon working electrode (5 mm inner diameter, 0.196 cm^2), a graphite rod counter electrode and an Ag/AgCl reference electrode were used for all the tests. All potentials in this work are relative to the reversible hydrogen electrode (RHE). The ink was prepared with 2 mg of catalyst, 20 μL of Nafion solution (5 %) and 1980 μL of isopropanol and ultrasonically mixed for 1 h. 20 μL of ink was pipetted on RDE and dried at ambient temperature. The CV measurements were performed in N$_2$-saturated 0.1 M HClO$_4$ solutions from 0.05 to 1.1 V vs. RHE at a scan rate of 50 mV s^{-1}. The LSV measurements were performed in O$_2$-saturated 0.1 M HClO$_4$ at a rotation rate of 1600 rpm and a sweep rate of 10 mV s^{-1} with iR-correction. The accelerated durability test (ADT) was carried out from 0.6 to 1.0 V vs. RHE with a scan rate of 100

mV s^{-1}. Before the electrochemical tests, all electrodes were pre-treated by cycling the potential between 0.05 and 1.10 V at a sweep rate of 50 mV s^{-1} for 100 cycles to remove surface contamination.

2.4. Membrane electrode assembly fabrication and fuel cell performance test

The ink for membrane electrode assembly preparation was similar to that for electrochemical test, which was ultrasonically sprayed onto Nafion 211 membrane at 90 °C. The active area of prepared catalyst-coated membranes (CCM) is 4 cm^2. Then, 230 μm thick carbon fiber films were pressed onto two sides of CCM at 120 °C for 90 s under a pressure of 1.5 MPa to obtain the MEA. The performance of MEA was characterized by a commercial fuel cell test system (Scribner 850e). The cell was operated at 80 °C with a back pressure of 150 kPa. Pure hydrogen and oxygen with 100 % relative humidity (RH) were supplied to the anode and cathode at a gas flow rate of 500–1000 sccm. The current-voltage polarization curves were recorded using potential step mode with 10 mV/point (holding 4 s for each point). The accelerated durability test (ADT) was conducted by applying cyclic sweeps from 0.6 V to 0.95 V with a sweep rate of 100 mV s^{-1} (H$_2$/N$_2$ 200/200 sccm). The mass activity was calculated based on the average current during the last 1 min at 0.9 V operated at 80 °C with a back pressure of 150 kPa after holding 15 min

2.5. DFT calculations

Density functional theory (DFT) was employed to calculate adsorption energies of oxygen species and free energy of oxygen reduction reaction using Vienna Ab-initio Simulation Package (VASP) software [37–39]. The Perdew-Burke-Ernzerhof (PBE) functional was adopted for all DFT calculations [40]. The projector augmented wave (PAW) method was used to describe the ionic cores with the energy cutoff of plane wave basis of 400 eV [41]. The convergence criterion of atomic structural optimization was set to 0.05 eV/Å. The (4×4) supercells of Pt(111), PtZn (111) and PtZn-skin(111) slabs were constructed with the vacuum layer thickness larger than 15 Å. The Brillouin zone was sampled with a k-mesh of (3×3×1). The electrode potential shift of Pt atom dissolution (ΔU_{Pt}) from PtZn-skin(111) slab compared with Pt atom from Pt(111) slab was calculated as:

$$\Delta U_{Pt} = -\frac{(E_{PtZn-skin(111)} - E'_{PtZn-skin(111)}) - (E_{Pt(111)} - E'_{Pt(111)})}{2e}$$

where $E_{PtZn-skin(111)}$ and $E_{Pt(111)}$ were the total energies of PtZn-skin (111) and Pt(111) slabs. $E'_{PtZn-skin(111)}$ and $E'_{Pt(111)}$ were the total energies of PtZn-skin(111) and Pt(111) slabs with a Pt atom vacancy [42, 43]. 2e was corresponded to the dissolution reaction of Pt - $2e = Pt^{2+}$. Note that positive ΔU_{Pt} means the enhanced stability of Pt atoms on the slab compared with Pt(111) slab. The computational hydrogen electrode model was performed to calculate the free energy diagram of oxygen reduction reaction on Pt(111) based slabs [44]. The ice-like bilayer water model was optimized on the slab to describe the interaction between slab and solution. The free energies of intermediates adsorbed on slab were calculated as:

$$\Delta G = \Delta E + \Delta ZPE - T\Delta S - neU + nk_B T \times pH \times \ln(10)$$

where ΔE and ΔZPE were calculated by total energies and zero point energies. ΔS was the change in entropy, which was calculated by considering the vibration frequencies of adsorbate. U was the electrode potential and pH was assumed to be zero for the acidic medium.

3. Results and discussion

3.1. Synthesis and structure characterization of the catalysts

Fig. 1a illustrates the synthetic route from carbon supported Pt nanoparticles (Pt/C) to PtZn intermetallic nanocrystals, the details of which are presented in the experimental section. In order to avoid the deposition of ZnO on carbon supports, Pt/C prepared by impregnation method is reduced at 600 ℃ to remove surface hydroxyl groups (Fig. S1). Moreover, O$_2$ is chosen as the oxygen source precursor and the ALD temperature is set as 80 °C to ensure the activation of O$_2$ on Pt nanoparticles. The thickness of ZnO shell can be regulated precisely by controlling the ALD cycles. As the XRD patterns shown in Fig. 1b, all samples have a same broad peak at around 25°, which could be attributed to the common carbon support [45,46]. Pt/C shows a typical face-centered cubic (fcc) crystal structure of Pt with diffraction peaks at 39.8° and 46.3°, which correspond to the (111) and (200) crystal planes, respectively. After 5 cycles ZnO coating on Pt/C labeled as Pt@ZnO/C, three peaks of ZnO located from 30° to 40° and the peak at 56.5° can be obviously observed. Then, the ordering reduction is performed at 800 °C, which drives the diffusion of Zn atoms in ZnO shell to alloy with Pt and form PtZn intermetallic nanocrystals (PtZn/C-ALD). The XRD pattern of PtZn/C-ALD shows that the signal of ZnO almost disappears and the diffraction peaks match well with that of the face-centered tetragonal (fct) L1$_0$-PtZn (PDF# 06–0604) [47]. Significantly, the partial enlarged XRD patterns show obvious shift of (111) and (200) planes of PtZn/C-ALD compared with those of Pt/C, indicating that Zn is incorporated into the Pt fcc structure to form an intermetallic phase with a concomitant lattice contraction.

Fig. 1c indicates that Pt nanoparticles are well dispersed on the surface of spherical carbon supports. The distance of the lattice fringes in Fig. 1d is about 0.226 nm, which is corresponding to the (111) facet of Pt. Compared with Pt/C, the morphology and distribution of Pt nanoparticles of Pt@ZnO/C in Fig. 1e are kept well. As the high-resolution transmission electron microscopy (HR-TEM) image shown in Fig. 1f, crystal ZnO shell with the thickness about 1 nm are observed coating on Pt nanoparticles. The electrochemical cyclic voltammetry (CV) measurements in Fig. S2 show that the ECSA of Pt in Pt@ZnO/C exhibits obvious reduction compared with that of Pt/C. Moreover, the HAADF-STEM images and corresponding elemental mappings of Pt@ZnO/C in Fig. 1g and Fig. S3 show the similar distribution of Pt and Zn elements, indicating ZnO is selectively deposited on Pt nanoparticles. As shown in Fig. 1h, the morphology of PtZn/C-ALD has no obvious change after high temperature reduction treatment. The HRTEM image of PtZn NPs in Fig. 1i shows that the measured inter-plane spacings are 0.221 nm and 0.202 nm, corresponding to the (111) and (200) crystal planes of L1$_0$-PtZn, respectively. As the elemental mappings of PtZn/C-ALD shown in Fig. 1j, homogenous Pt and Zn elements are highly overlapping, indicating that highly dispersed and ultra-small PtZn intermetallic nanocrystals are constructed after ordering reduction. As shown in Fig. 1k and Fig. S4, the average size of PtZn nanocrystals are 2.50 ± 0.65 nm, which is 0.63 nm larger than that of Pt/C (1.87 ± 0.38 nm) due to the reduction of ZnO shell. Since the protection of ZnO shell, the self-sintering of Pt nanoparticles is inhibited effectively and the narrow size distribution is kept. PtZn/C-ALD shows smaller average size and more uniform size distribution than the PtZn/C-IWI prepared by incipient wetness impregnation method (Fig. S5) and previously reported Pt-based intermetallic nanocrystals (Table S1).

3.2. Electronic structure and atomic coordination characterization

X-ray absorption fine structure (XAFS) was conducted to explore the nature of Pt species in Pt/C, Pt@ZnO/C and PtZn/C-ALD. As Fig. 2a displays, the Pt L$_3$-edge X-ray absorption near-edge structure (XANES) spectra of Pt/C, Pt@ZnO/C and PtZn/C-ALD fall in between those of PtO$_2$ and Pt foil, suggesting their different oxidized status of Pt [48–50].
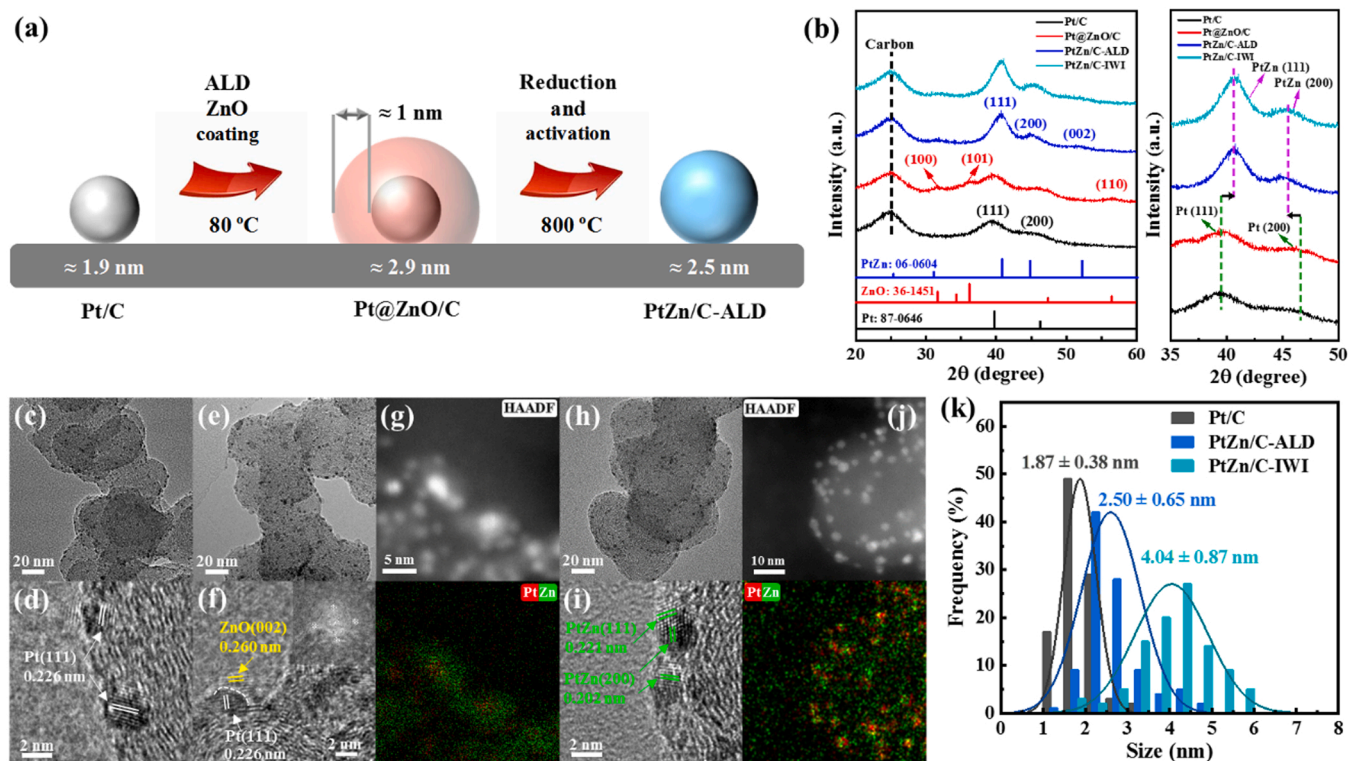
Fig. 1. (a) Schematic diagram of synthetic route. (b) XRD patterns and partial enlarged XRD patterns of the as-prepared Pt/C, Pt@ZnO/C, PtZn/C-ALD and PtZn/C-IWI. TEM image (c) and HR-TEM image (d) of Pt/C. TEM image (e) and HR-TEM image with corresponding fast Fourier transform image (f) of Pt@ZnO/C. (g) HAADF-STEM image and elemental mapping of Pt@ZnO/C. TEM image (h) and HR-TEM image (i) of PtZn/C-ALD. (j) HAADF-STEM image and elemental mapping of PtZn/C-ALD. (k) The nanoparticle size distribution of Pt/C, PtZn/C-ALD and PtZn/C-IWI.
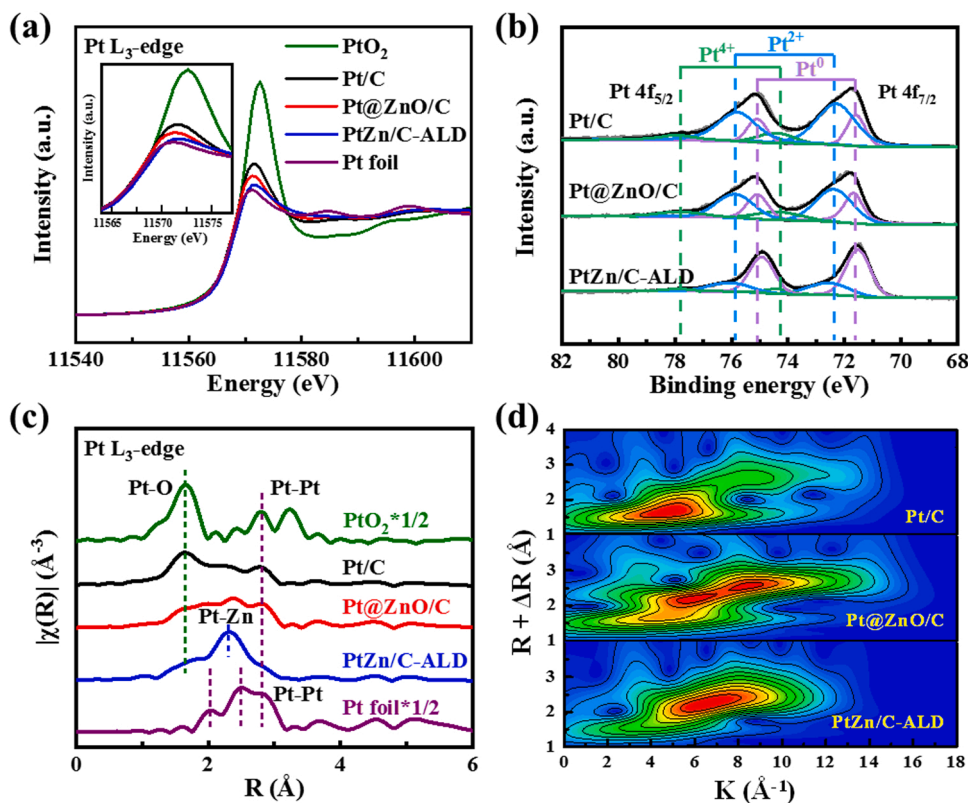

Fig. 2. (a) Pt L$_3$-edge XANES spectra of PtO$_2$ Pt/C, Pt@ZnO/C, PtZn/C-ALD and Pt foil with the corresponding enlarged view of the low energy region. (b) Pt 4f XPS analysis of Pt/C, Pt@ZnO/C and PtZn/C-ALD. (c) Pt L$_3$-edge k^2-weighted Fourier transform EXAFS spectra of PtO$_2$ Pt/C, Pt@ZnO/C, PtZn/C-ALD and Pt foil. (d) Wavelet transform EXAFS of Pt/C, Pt@ZnO/C and PtZn/C-ALD.

The inset in Fig. 2a shows that their white line peak intensities follow the sequence of Pt foil < PtZn/C-ALD < Pt@ZnO/C < Pt/C < PtO$_2$, indicating PtZn/C-ALD has the least content of oxidation state Pt compared with Pt@ZnO/C and Pt/C [10]. The Pt 4f X-ray photoelectron spectroscopy (XPS) analysis in Fig. 2b shows three valence states of Pt (Pt^{4+}, Pt^{2+} and Pt^0) exist in Pt/C, Pt@ZnO/C and PtZn/C-ALD, the relative concentrations of which are listed in Table S2. Pt/C shows very high oxidation state of Pt due to the interaction between Pt nanoparticles and carbon supports, which is similar to commercial Pt/C catalyst (Fig. S6). After ZnO coating, the wide XPS spectrum of Pt@ZnO/C shows obvious Zn 2p and O 1s signals (Fig. S7). The metallic state of Pt (31.7%) in Pt@ZnO/C is slightly higher than that of Pt/C (20.2%), which could be attributed to the partial reduction of Pt by diethylzinc precursor during ALD process and electron donor effect of ZnO shell [50]. Furthermore, Pt in PtZn/C-ALD shows large amounts of metallic Pt (66.1%) after high temperature reduction. The wide spectrum of XPS in Fig. S7 exhibits the decreased signals of Zn 2p and O 1s, implying the loss of Zn atoms during high temperature reduction, which also agrees well with the decreased mass concentration of Zn for PtZn/C-ALD (Table S3). Moreover, the binding energy of Pt^0 4$f_{7/2}$ peak reveals an obvious shift from 71.75 eV to 71.52 eV compared to Pt/C and Pt@ZnO/C, suggesting that the introduction of Zn brings out a down shift of the 5d-band center of Pt, which may be caused by the weaker electronegativity of Zn. As the XPS

spectra of Zn 2p shown in Fig. S8, although the proportion of Zn^0 increased after high temperature reduction, oxidized Zn still exists in the ultra-small PtZn intermetallic nanocrystals due to the electron transfer between Pt and Zn atoms.

The Fourier transform curves of extended X-ray absorption fine structure (EXAFS) are presented in Fig. 2c. Pt foil exhibits a typical first shell of Pt-Pt pair at 2.52 Å, while PtO$_2$ exhibits a typical Pt-O pair at 1.63 Å. From Pt/C, Pt@ZnO/C to PtZn/C-ALD, the signal of Pt-O pair becomes gradually weaker and the signal of Pt-Zn pair at 2.32 Å is getting stronger, confirming the formation of PtZn intermetallic nanocrystals [36]. EXAFS fitting in both R-space and k-space is further carried out to obtain the quantitative structural configuration of Pt in all samples in Fig. S9. As structural information listed in Table S4, the average coordination numbers of Pt-O follows the sequence of Pt/C > Pt@ZnO/C > PtZn/C-ALD. The sum of coordination numbers of Pt-Pt and Pt-Zn in PtZn/C-ALD is similar to that of Pt-Pt in Pt@ZnO/C, which is larger than that of Pt-Pt in Pt/C, indicating the reduction of Pt in the small Pt-based nanoparticles. The wavelet transform EXAFS analysis has also been provided to discriminate the backscattering atoms, which can reveal structural information in both k space and R space [51,52]. As shown in Fig. S10, the centers of wavelet transform EXAFS maxima for PtO$_2$ and Pt foil are located at 5.1 Å^{-1} and 8.6 Å^{-1}, which are assigned to Pt-O and Pt-Pt coordination, respectively. Fig. 2d shows that the
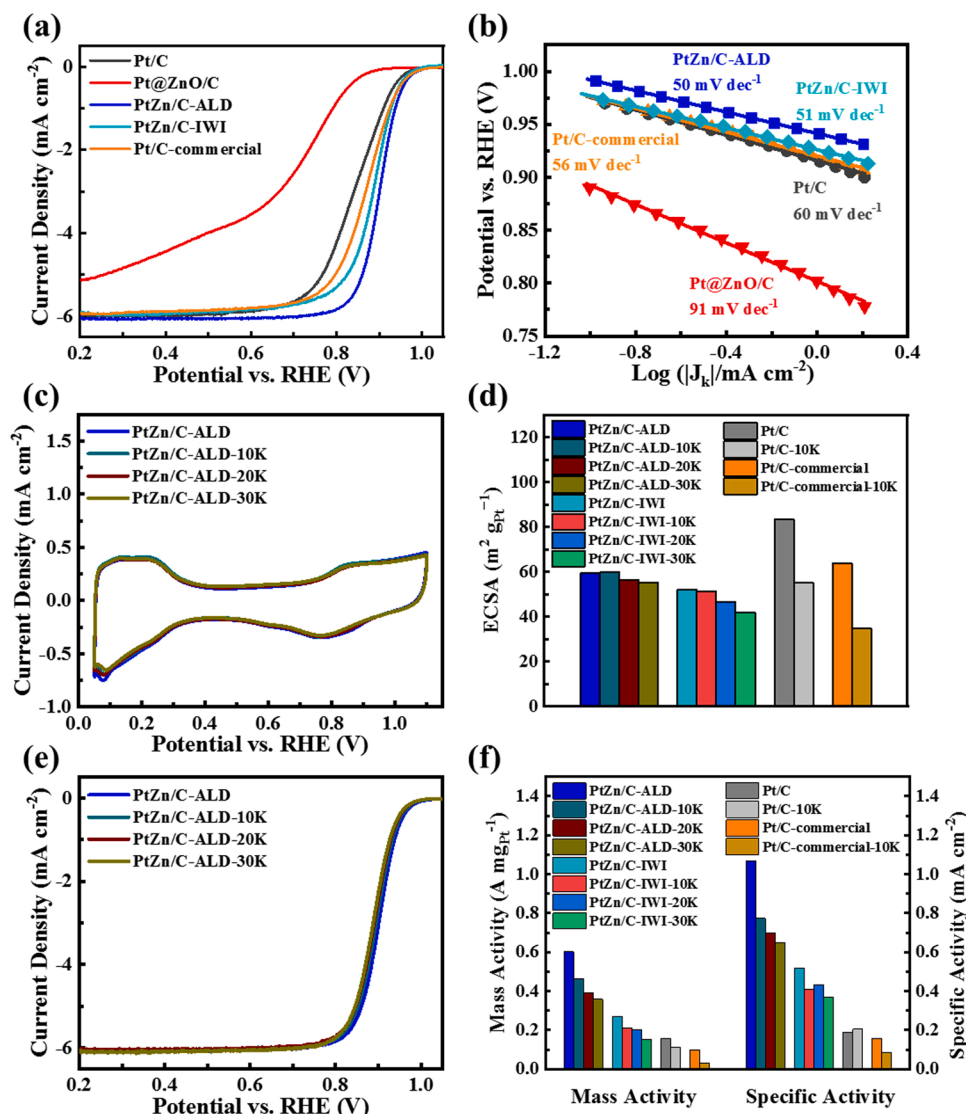

Fig. 3. (a) ORR polarization curves of Pt/C, Pt@ZnO/C, PtZn/C-ALD, PtZn/C-IWI and Pt/C-commercial. (b) Tafel curves of Pt/C, Pt@ZnO/C, PtZn/C-ALD, PtZn/C-IWI and Pt/C-commercial. (c) CV curves of PtZn/C-ALD before and after ADT. (d) ECSA changes of PtZn/C-ALD, PtZn/C-IWI, Pt/C and Pt/C commercial. (e) ORR polarization curves of PtZn/C-ALD before and after ADT. (f) Comparison of MA and SA for Pt/C, PtZn/C-ALD, PtZn/C-IWI and Pt/C-commercial at 0.9 V before and after ADT.

intensity maximum of Pt/C is near 4.9 Å^{-1} in k space, which could be ascribed to the Pt-O coordination. Pt@ZnO/C has two intensity maximum at 6.0 Å^{-1} and 8.3 Å^{-1} that caused by Pt-O and Pt-Pt coordination. As a comparison, the unique intensity maximum of PtZn/C-ALD located at 6.7 Å^{-1} could be attributed to the Pt-Zn scattering path.

3.3. Oxygen reduction performance evaluation

The ORR activity test has been performed by a rotating disk electrode (RDE) in O$_2$-saturated 0.1 M HClO$_4$ solution. Fig. 3a shows the polarization curves of Pt/C, Pt@ZnO/C, PtZn/C-ALD, PtZn/C-IWI and Pt/C-commercial electrocatalysts at 1600 revolutions per minute (rpm). The onset and half-wave potential (E$_{1/2}$) of our prepared Pt/C are 0.972 V and 0.842 V. The mass activity (MA) of Pt/C at 0.9 V is 0.15 A mg$_{Pt}^{-1}$, which is higher than that of Pt/C-commercial (Table S5). Since the formation of PtZn intermetallic nanocrystals, PtZn/C-IWI shows enhanced activity than Pt/C with the E$_{1/2}$ of 0.887 V and the MA of 0.27 A mg$_{Pt}^{-1}$. Since the surface Pt sites are covered by ZnO shell, the activity of Pt@ZnO/C shows obvious decline with the MA of 0.01 A mg$_{Pt}^{-1}$ at 0.9 V. After ordering reduction, PtZn/C-ALD shows a marked positive shift in E$_{1/2}$ of 34 mV relative to Pt/C-commercial. The MA and specific activity (SA) of PtZn/C-ALD reach to 0.60 A mg$_{Pt}^{-1}$ and 1.06 mA cm^{-2}, which are 6.0 and 6.8 times to Pt/C-commercial (0.10 A mg$_{Pt}^{-1}$ and 0.15 mA cm^{-2}) and rivals previously reported Pt-based intermetallic catalysts (Table S1). Furthermore, the Tafel curves are presented in Fig. 3b to analyze the kinetic activity of PtZn/C-ALD. Evidently, PtZn/C-ALD catalyst displays a smaller Tafel slope (50 mV dec^{-1}) than Pt/C (60 mV dec^{-1}), Pt/C-commercial (56 mV dec^{-1}) and PtZn/C-IWI (51 mV dec^{-1}). Moreover, the H$_2$O$_2$ yield during ORR catalyzed by PtZn/C-ALD shows the 1–2 % less than that of Pt/C-commercial, confirming a four-electron process of ORR on PtZn/C-ALD [53], which is consistent with the calculated electron transfer number from the Koutecky-Levich plots (Fig. S11 and Fig. S12).

The stability of PtZn/C-ALD is assessed by accelerated durability testing (ADT). In Fig. 3c, the CV curves of PtZn/C-ALD remain stable even after 30,000 cycles owing to its ordered structure. As a comparison, the ECSA of Pt/C and Pt/C-commercial show a drastic decrease after only 10,000 cycles as shown in Fig. S13. PtZn/C-IWI also shows relatively less stable than PtZn/C-ALD. In Fig. 3d, the calculated initial ECSA of PtZn/C-ALD is 59.43 m^2 g$_{Pt}^{-1}$. Interestingly, there is a slight increase of ECSA for PtZn/C-ALD after 10,000 cycles, which suggests that the Pt-rich surface is gradually formed with the leaching of Zn atoms on the surface of PtZn intermetallic nanocrystals. Even after 30,000 cycles, PtZn/C-ALD only exhibits a negligible loss in ECSA from 59.43 to 55.16 m^2 g$_{Pt}^{-1}$. PtZn/C-IWI shows a reduction in the ECSA from 52.11 to 41.65 m^2 g$_{Pt}^{-1}$ after 30,000 cycles. Especially, Pt/C-commercial suffers from severe ECSA degradation from 63.69 to 34.70 m^2 g$_{Pt}^{-1}$ with 45.51% loss after 10,000 cycles. The ORR polarization curves of PtZn/C-ALD after ADT have also been collected in Fig. 3e. PtZn/C-ALD demonstrates excellent stability with no obvious shift in E$_{1/2}$ after 10,000 potential cycles and a small negative shift around 13 mV even after 30,000 cycles. While PtZn/C-IWI face degradation with 21 mV loss of E$_{1/2}$, Pt/C-commercial and Pt/C face serious degradation with 51 mV and 57 mV loss of E$_{1/2}$ after only 10,000 cycles (Fig. S13). As shown in Fig. 3f, the MA of PtZn/C-ALD remains 0.46 A mg$_{Pt}^{-1}$ after 10,000 cycles, which is much higher than that of Pt/C-commercial (0.03 A mg$_{Pt}^{-1}$). Even after 30,000 potential cycles, the MA of PtZn/C-ALD remains 0.35 A mg$_{Pt}^{-1}$. The i-t testing under constant potential in O$_2$ saturated 0.1 M HClO$_4$ is also carried out. Fig. S14 shows the i-t curves of Pt/C-commercial and PtZn/C-ALD. It can be seen that after 10 h testing Pt/Zn/C-ALD exhibits the better stability with only 24.9% current loss far less than the 46.5% current loss of Pt/C-commercial.

Compared to Pt/C (Fig. S15), Pt/C-commercial (Fig. S16) and PtZn/C-IWI (Fig. S17), PtZn/C-ALD shows the best durability during ADT with a slight size increase of PtZn nanocrystals (Fig. 4a). Fig. 4b shows the HRTEM image of PtZn/C-ALD after ADT, the inter-plane spacing is still corresponding to the (111) crystal plane of L1$_0$-PtZn, indicating that the intermetallic structure of PtZn remains unchanged. The HAADF-STEM images and corresponding elemental mapping images of PtZn/C-ALD after ADT in Fig. 4c and Fig. S18 show that Pt and Zn atoms are simultaneously distributed over one single nanoparticle. Notably, the Pt mapping has a slightly larger area than the Zn mapping, indicating that a Pt-rich shell is formed at the surface of an ordered PtZn/C-ALD core with the gradual leaching of Zn atoms, which is in line with the increase of electrochemical active surface area for PtZn/C-ALD after 10,000 cycles
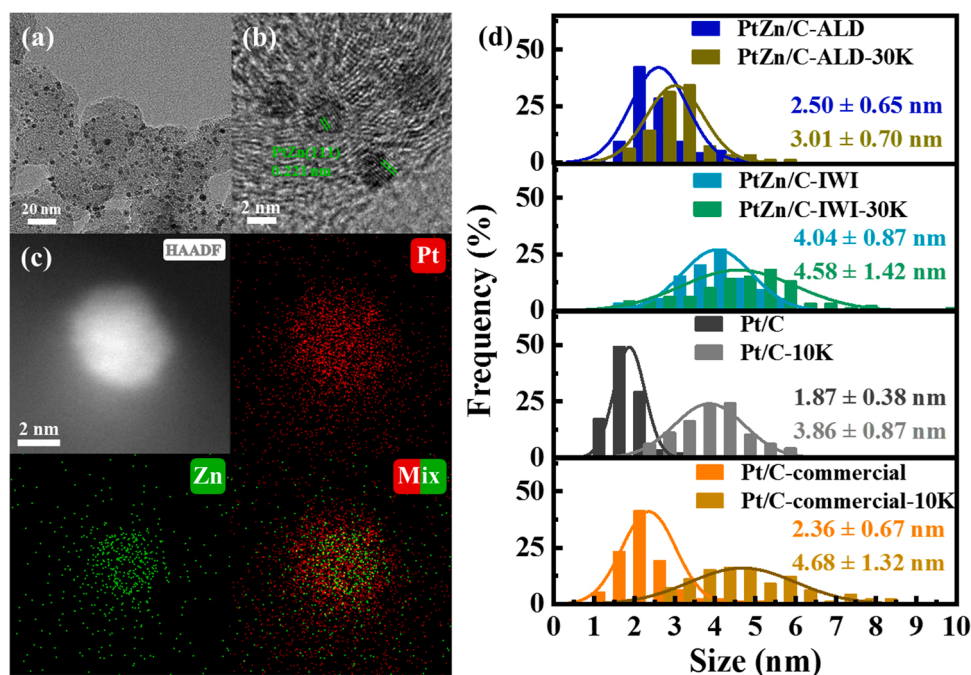

Fig. 4. (a) Low-resolution TEM image of PtZn/C-ALD after ADT. (b) HRTEM image of PtZn/C-ALD after ADT. (c) HAADF-STEM image and corresponding Elemental mapping images of PtZn/C-ALD after ADT. (d) Comparison of nanoparticle sizes for Pt/C, PtZn/C-ALD, PtZn/C-IWI and Pt/C-commercial before and after ADT.

and prove that the highly dispersed PtZn intermetallic nanocrystals is stable enough to resist ADT. As Fig. 4d displays, after 30,000 cycles ADT, the average size of PtZn/C-ALD nanocrystals is limited to 3.01 nm and significantly lower than those of Pt/C (3.86 nm), Pt/C-commercial (4.68 nm) and PtZn/C-IWI (4.58 nm) with narrower size distribution, indicating that PtZn/C-ALD has the highest ECSA even after ADT. Moreover, the narrow size distribution of PtZn intermetallic nanocrystals is kept with over 75% nanocrystals in the size range of 2.5–3.5 nm, implying the Ostwald ripening could be suppressed during electrochemical reaction.

3.4. Performance characterization in a fuel cell

To further evaluate the fuel cell performance of PtZn/C-ALD, a membrane electrode assembly has been fabricated by catalyst coated membrane method. Fig. 5a shows the current-voltage polarization curves of H_2-O_2 fuel cell at 80 °C for PtZn/C-ALD and Pt/C-commercial. PtZn/C-ALD (0.345 A cm^{-2}) exhibits an obvious larger current density compared to that of Pt/C-commercial (0.135 A cm^{-2}) at 0.8 V. The maximum peak power density of PtZn/C-ALD reaches to 1.56 W cm^{-2} with relatively lower Pt loading (0.07 mg$_{Pt}$ cm^{-2}), which is 1.26 times that of Pt/C-commercial cathode (1.24 W cm^{-2}, 0.14 mg$_{Pt}$ cm^{-2}). When feeding with air, PtZn/C-ALD also exhibits observably higher cell voltages at various current densities compared to Pt/C-commercial in Fig. 5b, indicating the greatly enhanced ORR activity and mass transportation. The maximum peak power density of PtZn/C-ALD is about 0.63 W cm^{-2} and 0.51 W cm^{-2} for Pt/C-commercial. As shown in Fig. 5c, the maximum peak power density loss of PtZn/C-ALD is only 81 mW cm^{-2} after 30,000 voltage cycles, exhibiting better stability than Pt/C-commercial (Fig. S19, 175 mW cm^{-2} loss). As the MA before and after voltage cycles shown in Fig. 5d, the initial MA of PtZn/C-ALD is 0.48 A mg$_{Pt}^{-1}$, which is better than the U.S. Department of Energy (DOE) 2020 targets of fuel cell (begin of life: 0.44 A mg$_{Pt}^{-1}$) [54,55]. The MA of PtZn/C-ALD after 30,000 cycles remains 0.43 A mg$_{Pt}^{-1}$ with the loss of 10.42 %, which can also meet the DOE 2020 targets at the end of life (0.26 A mg$_{Pt}^{-1}$). The single cell performance of PtZn/C-ALD is superior to that of commercial Pt/C (0.20 A mg$_{Pt}^{-1}$, 40.04 % MA loss) and rivals state-of-the-art Pt-based intermetallic nanocrystals (Table S6).

3.5. Theoretical understanding of the enhanced activity and durability

Density functional theory (DFT) calculations have been employed to further reveal the mechanism of enhanced ORR activity and stability of ordered PtZn intermetallic nanocrystals. Fig. S20 shows the ideal slab models of (111) surface of pure Pt and PtZn. Since the surface Zn atoms on PtZn(111) could be dissolve in actual acidic electrolyte as the ESCA increases for PtZn/C-ALD after 10,000 cycles, a model of PtZn(111) with an additional layer of Pt atoms designated as PtZn-skin(111) is constructed as shown in Fig. 6a. The Pt-Pt bond lengths along [101] and [011] directions (2.71 Å and 2.69 Å) in the Pt skin of PtZn-skin(111) are shorter than that of Pt(111) (2.81 Å) and PtZn(111) (2.87 Å) (Fig. S20), which can be attributed to the lattice mismatch between PtZn(111) core and Pt skin. The calculated electrode potential shifts of Pt atoms on PtZn-skin(111) are 0.06 V and 0.15 V with respect to Pt(111), indicating that the Pt atoms on PtZn-skin(111) are more stable than Pt on Pt(111), which also agrees well with the excellent stability of PtZn/C-ALD. The negative bader charges of Pt atoms and positive bader charges of Zn atoms in the same layer can be attributed to the lower electronegativity of Zn compared to Pt, which are consistent with the XPS results. The atomic structures of Pt(111), PtZn(111) and PtZn-skin(111) after O_2 molecule and O atom adsorption are displayed in Fig. S21 and Fig. S22. Fig. 6b shows that PtZn-skin(111) exhibits much lower O_2 molecule and O atom adsorption energies than Pt(111) and PtZn(111) due to the compression strain of Pt skin on PtZn(111). The free energy diagrams of ORR intermediate processes on Pt(111), PtZn-skin(111) and PtZn(111) are presented in Fig. 6c with the optimized structures of reaction intermediates during ORR shown in Figs. S23-S25. According to the free energy diagram at equilibrium potential (1.23 V), the free energy change of the rate-limited step for PtZn-skin(111) is 0.45 eV, which is much lower than that of Pt(111) (0.60 eV) and PtZn(111) (0.88 eV). The lower free energy change of PtZn-skin(111) agrees well with the high activity of PtZn/C-ALD catalyst, which is attributed to the weak adsorption of O atom due to the weak polarization of surface Pt atoms compared with that on Pt(111) (Fig. 6d and Fig. S26).

4. Conclusion

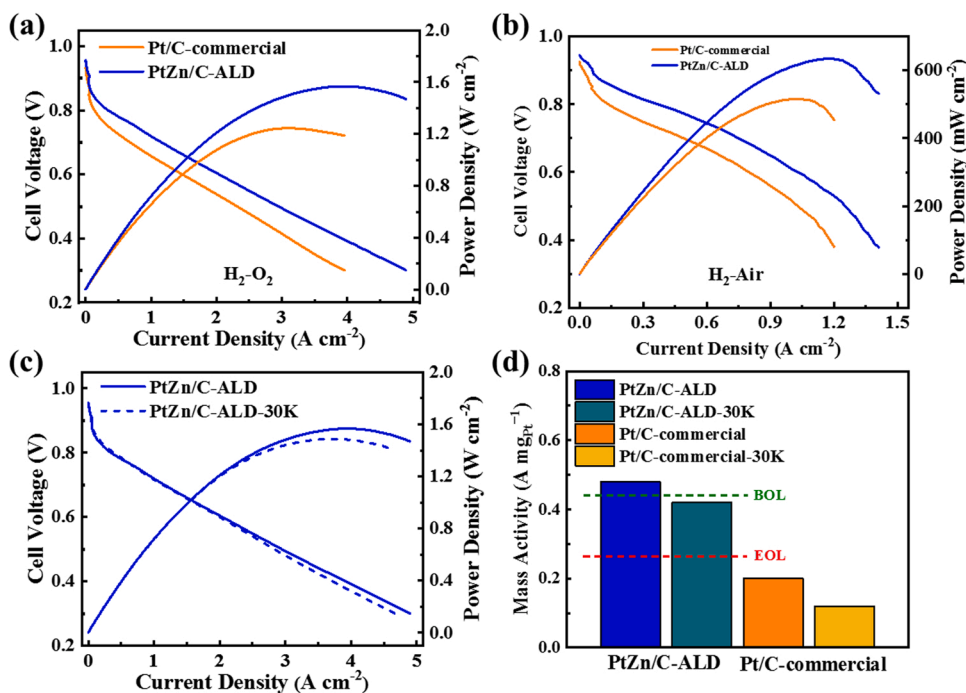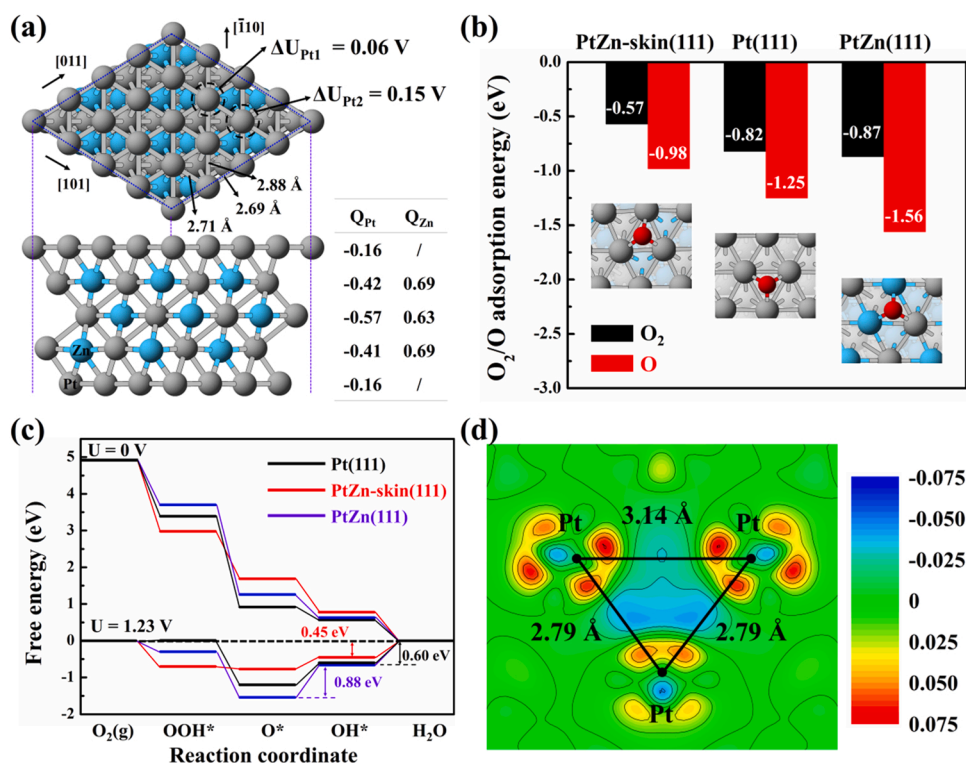In summary, we have developed a construction method to prepare

Fig. 5. (a) H_2-O_2 fuel cell polarization curves of PtZn/C-ALD and Pt/C-commercial. (b) H_2-Air fuel cell polarization curves of PtZn/C-ALD and Pt/C-commercial. (c) H_2-O_2 fuel cell polarization curves of PtZn/C-ALD before and after 30,000 voltage cycles. (Anode: 0.1 mg$_{Pt}$ cm^{-2} Pt/C-commercial; cathode: 0.07 mg$_{Pt}$ cm^{-2} PtZn/C-ALD or 0.14 mg$_{Pt}$ cm^{-2} Pt/C-commercial; membrane: Nafion 211; temperature: 80 °C; backpressure: 150 kPa; relative humidity: 100%). (d) Changes of MA of PtZn/C-ALD and Pt/C-commercial before and after voltage cycles (green and red dash lines indicate the DOE beginning-of-life (BOL) and end-of-life (EOL) targets, respectively).

Fig. 6. (a) Atomic structure of PtZn-skin(111) slab. The calculated electrode potential shift of surface Pt atoms (ΔU_{Pt1} and ΔU_{Pt2}) with respect to the potential of Pt(111), as well as average bader charges of Pt atoms and Zn atoms in the same layer (Q_{Pt} and Q_{Zn}) have been labeled. (b) O_2 molecule and O atom adsorption energies on PtZn-skin(111), Pt(111) and PtZn(111) slabs. (c) Calculated free energy diagrams of ORR on Pt(111), PtZn-skin(111) and PtZn(111) under 0 V and 1.23 V vs. RHE. (d) Contours of the differential charge density in the plane crossing surface Pt atoms for O atom adsorbed PtZn-skin (111).

highly dispersed Pt-based intermetallic nanocrystals with controllable size and uniform size distribution. The method is based on the selectively ultra-thin metal oxide coating on Pt nanoparticles via ALD and subsequently fast ordering reduction, in which the metal oxide coating can not only provide metal atoms for alloying, but also prevent the sintering of Pt nanoparticles during ordering. The prepared uniform ultra-small PtZn intermetallic nanocrystals exhibit enhanced activity and stability for fuel cell ORR compared to commercial Pt/C, which is attributed to the decreased binding energy of Pt-oxygen intermediates and suppressed electrochemical Ostwald ripening. This work serves as a promising method to precisely control the size and distribution of Pt-based intermetallic nanocrystals.

CRediT authorship contribution statement

Chaojun Huang: Investigation, Formal analysis, Writing-Original Draft. **Dr. Hang Liu**: Validation, Data Curation, Writing-Original Draft. **Dr. Yuanting Tang**: Investigation. **Qizi Lu**: Formal analysis. **Dr. Shengqi Chu**: Data Curation. **Dr.** Xiao Liu: Data Curation, Writing-Review & Editing, Visualization. Prof. Bin Shan: Resources, Project administration. Prof. Rong Chen: Writing-Review & Editing, Visualization, Resources, Funding acquisition.

Declaration of Competing Interest

The authors declare that they have no known competing financial interests or personal relationships that could have appeared to influence the work reported in this paper.

Data availability

Data will be made available on request.

Acknowledgments

Author Contributions

Chaojun Huang and Hang Liu contributed equally to this work. Chaojun Huang and Hang Liu conducted the synthesis and characterizations of catalysts and wrote the paper. Yuanting Tang performed TEM characterizations. Chaojun Huang and Qizi Lu performed catalytic activity evaluation. Xiao Liu was responsible for the detailed DFT calculations. Shengqi Chu performed XAFS characterizations. Xiao Liu, Bin Shan and Rong Chen directed the project and mentored the paper writing. All authors discussed the results and commented on the paper.

Appendix A. Supporting information

Supplementary data associated with this article can be found in the online version at doi:10.1016/j.apcatb.2022.121986.

References

[1] K. Jiao, J. Xuan, Q. Du, Z. Bao, B. Xie, B. Wang, Y. Zhao, L. Fan, H. Wang, Z. Hou, S. Huo, N.P. Brandon, Y. Yin, M.D. Guiver, Designing the next generation of proton-exchange membrane fuel cells, Nature 595 (2021) 361–369.

[2] J. Guan, S. Yang, T. Liu, Y. Yu, J. Niu, Z. Zhang, F. Wang, Intermetallic FePt@PtBi core-shell nanoparticles for oxygen reduction electrocatalysis, Angew. Chem. Int. Ed. 60 (2021) 21899–21904.

[3] Z. Zhao, C. Chen, Z. Liu, J. Huang, M. Wu, H. Liu, Y. Li, Y. Huang, Pt-based nanocrystal for electrocatalytic oxygen reduction, Adv. Mater. 31 (2019), 1808115.

[4] B. Shen, L. Huang, J. Shen, K. He, C.Y. Zheng, V.P. Dravid, C. Wolverton, C. A. Mirkin, Crystal structure engineering in multimetallic high-index facet nanocatalysts, Proc. Natl. Acad. Sci. USA 118 (2021), e2105722118.

[5] Y. Xiong, Y. Yang, F.J. DiSalvo, H.D. Abruña, Synergistic bimetallic metallic organic framework-derived Pt-Co oxygen reduction electrocatalysts, ACS Nano 14 (2020) 13069–13080.

[6] J. Li, Z. Xi, Y.T. Pan, J.S. Spendelow, P.N. Duchesne, D. Su, Q. Li, C. Yu, Z. Yin, B. Shen, Y.S. Kim, P. Zhang, S. Sun, Fe stabilization by intermetallic L1₀-FePt and Pt catalysis enhancement in L1₀-FePt/Pt nanoparticles for efficient oxygen reduction reaction in fuel cells, J. Am. Chem. Soc. 140 (2018) 2926–2932.

[7] C. Wang, X. Sang, J.T.L. Gamler, D.P. Chen, R.R. Unocic, S.E. Skrabalak, Facet-dependent deposition of highly strained alloyed shells on intermetallic nanoparticles for enhanced electrocatalysis, Nano Lett. 17 (2017) 5526–5532.

[8] Y. Xiong, L. Xiao, Y. Yang, F.J. DiSalvo, H.D. Abruña, High-loading intermetallic Pt₃Co/C core–shell nanoparticles as enhanced activity electrocatalysts toward the oxygen reduction reaction (ORR), Chem. Mater. 30 (2018) 1532–1539.

[9] X. Zhao, C. Xi, R. Zhang, L. Song, C. Wang, J.S. Spendelow, A.I. Frenkel, J. Yang, H. L. Xin, K. Sasaki, High-performance nitrogen-doped intermetallic PtNi catalyst for the oxygen reduction reaction, ACS Catal. 10 (2020) 10637–10645.

[10] M. Liu, B.A. Lu, G. Yang, P. Yuan, H. Xia, Y. Wang, K. Guo, S. Zhao, J. Liu, Y. Yu, W. Yan, C.L. Dong, J.N. Zhang, S. Mu, Concave Pt-Zn nanocubes with high-index faceted Pt skin as highly efficient oxygen reduction catalyst, Adv. Sci. 9 (2022), 2200147.

[11] S. Zaman, L. Huang, A.I. Douka, H. Yang, B. You, B.Y. Xia, Oxygen reduction electrocatalysts toward practical fuel cells: progress and perspectives, Angew. Chem. Int. Ed. 60 (2021) 17832–17852.

[12] X. Zhao, H. Cheng, L. Song, L. Han, R. Zhang, G. Kwon, L. Ma, S.N. Ehrlich, A. I. Frenkel, J. Yang, K. Sasaki, H.L. Xin, Rhombohedral ordered intermetallic nanocatalyst boosts the oxygen reduction reaction, ACS Catal. 11 (2021) 184–192.

[13] M. Gong, D. Xiao, Z. Deng, R. Zhang, W. Xia, T. Zhao, X. Liu, Y. Hu, Y. Lu, X. Zhao, H. Xin, D. Wang, Structure evolution of PtCu nanoframes from disordered to ordered for the oxygen reduction reaction, Appl. Catal. B-Environ. 282 (2021), 119617.

[14] M. Luo, Y. Sun, L. Wang, S. Guo, Tuning multimetallic ordered intermetallic nanocrystals for effcient energy electrocatalysis, Adv. Energy Mater. 7 (2017), 1602073.

[15] X. Chen, S. Zhang, C. Li, Z. Liu, X. Sun, S. Cheng, D.N. Zakharov, S. Hwang, Y. Zhu, J. Fang, G. Wang, G. Zhou, Composition-dependent ordering transformations in Pt-Fe nanoalloys, Proc. Natl. Acad. Sci. USA 119 (2022), e2117899119.

[16] J. Cao, H. Cao, F. Wang, H. Zhu, Fully ordered L1₀-PtCoAu electrocatalyst derived from PtAu@CoO precursor with enhanced performance for oxygen reduction reaction, Electrochim. Acta 384 (2021), 138266.

[17] Z. Wang, X. Yao, Y.L. Miao, D. Xia, L. Gan, Structurally ordered low-Pt intermetallic electrocatalysts toward durably high oxygen reduction reaction activity, Adv. Funct. Mater. 29 (2019), 1902987.

[18] T.Y. Yoo, J.M. Yoo, A.K. Sinha, M.S. Bootharaju, E. Jung, H.S. Lee, B.H. Lee, J. Kim, W.H. Antink, Y.M. Kim, J. Lee, E. Lee, D.W. Lee, S.P. Cho, S.J. Yoo, Y.E. Sung, T. Hyeon, Direct synthesis of intermetallic platinum-alloy nanoparticles highly loaded on carbon supports for efficient electrocatalysis, J. Am. Chem. Soc. 142 (2020) 14190–14200.

[19] X. Zhu, X. Tan, K. Wu, S. Haw, C. Pao, B. Su, J. Jiang, S.C. Smith, J. Chen, R. Amal, X. Lu, Intrinsic ORR activity enhancement of Pt atomic sites by engineering the d-band center via local coordination tuning, Angew. Chem. Int. Ed. 60 (2021) 21911–21917.

[20] Q. Luo, W. Xu, S. Tang, Fabricating high-loading ultra-small PtCu₃/rGO via a traceless protectant and spray-freeze-drying method, Appl. Catal. B-Environ. 312 (2022), 121433.

[21] H. Cheng, R. Gui, H. Yu, C. Wang, S. Liu, H. Liu, T. Zhou, N. Zhang, X. Zheng, W. Chu, Y. Lin, H. Wu, C. Wu, Y. Xie, Subsize Pt-based intermetallic compound enables long-term cyclic mass activity for fuel-cell oxygen reduction, Proc. Natl. Acad. Sci. USA 118 (2021), e2104026118.

[22] P. Yin, X. Luo, Y. Ma, S. Chu, S. Chen, X. Zheng, J. Lu, X. Wu, H. Liang, Sulfur stabilizing metal nanoclusters on carbon at high temperatures, Nat. Commun. 12 (2021) 3135.

[23] L. Wang, M. Chen, Q. Yan, S. Xu, S. Chu, P. Chen, Y. Lin, H. Liang, A sulfur-tethering synthesis strategy toward high-loading atomically dispersed noble metal catalysts, Sci. Adv. 5 (2019), eaax6322.

[24] W.W. McNeary, S.F. Zaccarine, A. Lai, A.E. Linico, S. Pylypenko, A.W. Weimer, Improved durability and activity of Pt/C catalysts through atomic layer deposition of tungsten nitride and subsequent thermal treatment, Appl. Catal. B-Environ. 254 (2019) 587–593.

[25] C. Yang, L. Wang, P. Yin, J. Liu, M. Chen, Q. Yan, Z. Wang, S. Xu, S. Chu, C. Cui, H. Ju, J. Zhu, Y. Lin, J. Shui, H. Liang, Sulfur-anchoring synthesis of platinum intermetallic nanoparticle catalysts for fuel cells, Science 374 (2021) 459–464.

[26] Y. Ma, A.N. Kuhn, W. Gao, T. Zoubi, H. Du, X. Pan, H. Yang, Strong electrostatic adsorption approach to the synthesis of sub-three nanometer intermetallic platinum-cobalt oxygen reduction catalysts, Nano Energy 79 (2021), 105465.

[27] M. Xu, Y. Zhao, H. Chen, W. Ni, M. Liu, S. Huo, L. Wu, X. Zang, Z. Yang, Y. Yan, Role of ultrathin carbon shell in enhancing the performance of PtZn intermetallic nanoparticles as an anode electrocatalyst for direct formic acid fuel cells, ChemElectroChem 6 (2019) 2316–2323.

[28] X.X. Wang, S. Hwang, Y. Pan, K. Chen, Y. He, S. Karakalos, H. Zhang, J. S. Spendelow, D. Su, G. Wu, Ordered Pt₃Co intermetallic nanoparticles derived from metal-organic frameworks for oxygen reduction, Nano Lett. 18 (2018) 4163–4171.

[29] Y. Hu, T. Shen, X. Zhao, J. Zhang, Y. Lua, J. Shen, S. Lu, Z. Tu, H.L. Xin, D. Wang, Combining structurally ordered intermetallics with N-doped carbon confinement

[30] for efficient and anti-poisoning electrocatalysis, Appl. Catal. B-Environ. 279 (2020), 119370.

[30] J. Kim, Y. Lee, S. Sun, Structurally ordered FePt nanoparticles and their enhanced catalysis for oxygen reduction reaction, J. Am. Chem. Soc. 132 (2010) 4996–4997.

[31] Z. Yang, H. Yang, L. Shang, T. Zhang, Ordered PtFeIr intermetallic nanowires prepared through a silica-protection strategy for the oxygen reduction reaction, Angew. Chem. Int. Ed. 61 (2022), e202113278.

[32] B. Zhang, G. Fu, Y. Li, L. Liang, N.S. Grundish, Y. Tang, J.B. Goodenough, Z. Cui, General strategy for synthesis of ordered Pt₃M intermetallics with ultrasmall particle size, Angew. Chem. Int. Ed. 59 (2020) 7857–7863.

[33] X. Li, Y. He, S. Cheng, B. Li, Y. Zeng, Z. Xie, Q. Meng, L. Ma, K. Kisslinger, X. Tong, S. Hwang, S. Yao, C. Li, Z. Qiao, C. Shan, Y. Zhu, J. Xie, G. Wang, G. Wu, D. Su, Atomic structure evolution of Pt-Co binary catalysts: single metal sites versus intermetallic nanocrystals, Adv. Mater. 33 (2021), 2106371.

[34] T. Wang, J. Liang, Z. Zhao, S. Li, G. Lu, Z. Xia, C. Wang, J. Luo, J. Han, C. Ma, Y. Huang, Q. Li, Sub-6 nm fully ordered L1₀-Pt-Ni-Co nanoparticles enhance oxygen reduction via co doping induced ferromagnetism enhancement and optimized surface strain, Adv. Energy Mater. 9 (2019), 1803771.

[35] H. Lee, J.E. Park, O.H. Kim, W. Hwang, H.J. Choi, J.C. Yang, C.Y. Ahn, M.S. Lim, I. Choi, Y.H. Cho, Y.E. Sung, Boosting electrochemical stability of ultralow-Pt nanoparticle with Matryoshka-like structure in polymer electrolyte membrane fuel cells, Appl. Catal. B-Environ. 268 (2020), 118450.

[36] J. Liang, N. Li, Z. Zhao, L. Ma, X. Wang, S. Li, X. Liu, T. Wang, Y. Du, G. Lu, J. Han, Y. Huang, D. Su, Q. Li, Tungsten-doped L1₀-PtCo ultrasmall nanoparticles as a high-performance fuel cell cathode, Angew. Chem. Int. Ed. 58 (2019) 15471–15477.

[37] G. Kresse, J. Hafner, Ab initio molecular dynamics for liquid metals, Phys. Rev. B 47 (1993) 558–561.

[38] G. Kresse, J. Hafner, Ab initio molecular-dynamics simulation of the liquid-metal-amorphous-semiconductor transition in germanium, Phys. Rev. B 49 (1994) 14251–14269.

[39] G. Kresse, J. Furthmüller, Efficiency of ab-initio total energy calculations for metals and semiconductors using a plane-wave basis set, Comput. Mater. Sci. 6 (1996) 15–50.

[40] J.P. Perdew, K. Burke, M. Ernzerhof, Generalized gradient approximation made simple, Phys. Rev. Lett. 77 (1996) 3865–3868.

[41] G. Kresse, D. Joubert, From ultrasoft pseudopotentials to the projector augmented-wave method, Phys. Rev. B 59 (1999) 1758–1775.

[42] J. Greeley, J.K. Nørskov, Electrochemical dissolution of surface alloys in acids: thermodynamic trends from first-principles calculations, Electrochim. Acta 52 (2007) 5829–5836.

[43] Y. Ma, P.B. Balbuena, Surface properties and dissolution trends of Pt₃M alloys in the presence of adsorbates, J. Phys. Chem. C 112 (2008) 14520–14528.

[44] J.K. Nørskov, J. Rossmeisl, A. Logadottir, L. Lindqvist, J.R. Kitchin, T. Bligaard, H. Jónsson, Origin of the overpotential for oxygen reduction at a fuel-cell cathode, J. Phys. Chem. B 108 (2004) 17886–17892.

[45] D.Z. Khater, R.S. Amin, M. Mahmoud, K.M. El-Khatib, Evaluation of mixed transition metal (Co, Mn, and Cu) oxide electrocatalysts anchored on different carbon supports for robust oxygen reduction reaction in neutral media, RSC Adv. 12 (2022) 2207–2218.

[46] D.N. Futaba, T. Yamada, K. Kobashi, M. Yumura, K. Hata, Macroscopic wall number analysis of single-walled, double-walled, and few-walled carbon nanotubes by X-ray diffraction, J. Am. Chem. Soc. 133 (2011) 5716–5719.

[47] J. Liang, Z. Zhao, N. Li, X. Wang, S. Li, X. Liu, T. Wang, G. Lu, D. Wang, B. J. Hwang, Y. Huang, D. Su, Q. Li, Biaxial strains mediated oxygen reduction electrocatalysis on Fenton reaction resistant L1₀-PtZn fuel cell cathode, Adv. Energy Mater. 10 (2020), 2000179.

[48] B. Ravel, M. Newville, ATHENA, ARTEMIS, HEPHAESTUS: data analysis for X-ray absorption spectroscopy using IFEFFIT, J. Synchrotron Rad. 12 (2005) 537–541.

[49] X. Liu, S. Jia, M. Yang, Y. Tang, Y. Wen, S. Chu, J. Wang, B. Shan, R. Chen, Activation of subnanometric Pt on Cu-modified CeO₂ via redox-coupled atomic layer deposition for CO oxidation, Nat. Commun. 11 (2020) 4240.

[50] A. Han, J. Zhang, W. Sun, W. Chen, S. Zhang, Y. Han, Q. Feng, L. Zheng, L. Gu, C. Chen, Q. Peng, D. Wang, Y. Li, Isolating contiguous Pt atoms and forming Pt-Zn intermetallic nanoparticles to regulate selectivity in 4-nitrophenylacetylene hydrogenation, Nat. Commun. 10 (2019) 3787.

[51] X. Yang, Y. Wang, X. Wang, B. Mei, E. Luo, Y. Li, Q. Meng, Z. Jin, Z. Jiang, C. Liu, J. Ge, W. Xing, CO-tolerant PEMFC anodes enabled by synergistic catalysis between iridium single-atom sites and nanoparticles, Angew. Chem. Int. Ed. 60 (2021) 26177–26183.

[52] Y. Cao, H. Peng, S. Chu, Y. Tang, C. Huang, Z. Wang, F. Liu, J. Wu, B. Shan, R. Chen, Molten-salt-assisted thermal emitting method to transform bulk Fe₂O₃ into Fe single atom catalysts for oxygen reduction reaction in Zn-air battery, Chem. Eng. J. 420 (2021), 129713.

[53] D. Wang, H.L. Xin, R. Hovden, H. Wang, Y. Yu, D.A. Muller, F.J. DiSalvo, H. D. Abruña, Structurally ordered intermetallic platinum-cobalt core-shell nanoparticles with enhanced activity and stability as oxygen reduction electrocatalysts, Nat. Mater. 12 (2013) 81–87.

[54] US DOE fuel cell Technologies Office, multi-year research, development & demonstration plan: fuel cells. https://www.energy.gov/sites/prod/files/2017/05/f34/fcto_myrdd_fuel_cells.pdf, (2017).

[55] S.M. Dull, O. Vinogradova, S. Xu, D.M. Koshy, P.E. Vullum, J. Torgersen, S. Kirsch, V. Viswanathan, T.F. Jaramillo, F.B. Prinz, Alloyed Pt-Zn oxygen reduction catalysts for proton exchange membrane fuel cells, ACS Appl. Energy Mater. 5 (2022) 8282–8291.